



저작자표시-비영리-변경금지 2.0 대한민국

이용자는 아래의 조건을 따르는 경우에 한하여 자유롭게

- 이 저작물을 복제, 배포, 전송, 전시, 공연 및 방송할 수 있습니다.

다음과 같은 조건을 따라야 합니다:



저작자표시. 귀하는 원저작자를 표시하여야 합니다.



비영리. 귀하는 이 저작물을 영리 목적으로 이용할 수 없습니다.



변경금지. 귀하는 이 저작물을 개작, 변형 또는 가공할 수 없습니다.

- 귀하는, 이 저작물의 재이용이나 배포의 경우, 이 저작물에 적용된 이용허락조건을 명확하게 나타내어야 합니다.
- 저작권자로부터 별도의 허가를 받으면 이러한 조건들은 적용되지 않습니다.

저작권법에 따른 이용자의 권리는 위의 내용에 의하여 영향을 받지 않습니다.

이것은 [이용허락규약\(Legal Code\)](#)을 이해하기 쉽게 요약한 것입니다.

[Disclaimer](#)

Master Thesis

Cryogenic Mechanical Properties and Microstructure of CrCoNi
Medium Entropy Alloy Processed by Selective Laser Melting

The Graduate School
of the University of Ulsan
School of Mechanical Engineering

Nguyen Tri Hoang

Cryogenic Mechanical Properties and Microstructure of CrCoNi
Medium Entropy Alloy Processed by Selective Laser Melting

Supervisor: Prof. Doo-Man Chun
Co-advisor: Prof. Dong-Kyu Kim

A Thesis

Submitted to
The Graduate School of the University of Ulsan
In partial Fulfillment of the Requirements
For the Degree of

Master of Science

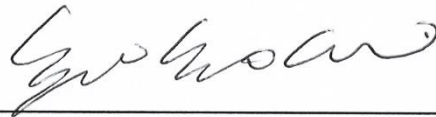
by

Nguyen Tri Hoang

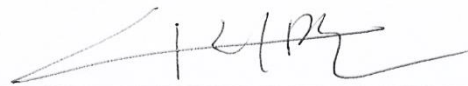
School of Mechanical Engineering
Ulsan, Korea
August 2022

Cryogenic Mechanical Properties and Microstructure of CrCoNi
Medium Entropy Alloy Processed by Selective Laser Melting

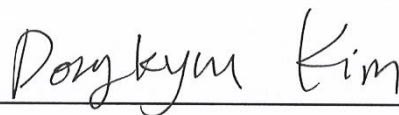
This certifies that the thesis of Nguyen Tri Hoang is approved



Committee Chair Kyoungsik Chang



Committee Member Doo-Man Chun



Committee Member Dong-Kyu Kim

Ulsan, Korea

August 2022

ACKNOWLEDGMENT

First and foremost, I would like to express my sincere gratitude to Prof. Doo Man Chun and Prof. Dong-Kyu Kim for their enthusiasm and immense knowledge. Their guidance helped me in all the time of research and writing of this thesis. I am really lucky to have had an opportunity to work as a their graduate.

I thank my fellow labmates in Computational Advanced Materials Processing Laboratory: Tran Minh Tien, Zhengtong Shan, Pham Minh Sang, Lee Dae-Ho, for enlightening me the first glance of research, for supporting me in my daily life, for the stimulating discussions and for all the fun we have had in the last two years.

Last but not the least, I also take this opportunity to express a deep sense of gratitude to all employees and Professors at the Department of Mechanical Engineering, University of Ulsan for their wonderful work.

ABSTRACT

The present study investigated the cryogenic mechanical properties and microstructure of CrCoNi medium entropy alloy (MEA) fabricated by selective laser melting (SLM) with hot isostatic pressing (HIP). The SLM processing parameters were optimized with respect to the relative density and micro-hardness of as-built CrCoNi specimens. The microstructure and mechanical properties of CrCoNi MEA fabricated with the optimal SLM processing parameters were characterized by uniaxial tensile test, electron backscatter diffraction (EBSD) and transmission electron microscopy (TEM) at room (298 K) and cryogenic (150 K) temperatures. At 150 K, both strength and ductility of SLM CrCoNi MEA are noticeably increased compared to room temperature (yield strength increased by 6.5% and ductility by 10.0% for as-built specimen, those of HIP treated specimen increased by 22.7% and 6.6%, respectively). The HIP treated CrCoNi reveals the considerable improvement of ductility at both temperatures compared to the as-built one (90.0% and 84.1% at room and cryogenic temperatures, respectively). The high cooling rate of 3.2×10^6 K/s obtained from the simulation may result in the fine microstructure and high dislocation density, accordingly the high yield strength of SLM CrCoNi MEA. The high ductility of SLM CrCoNi MEA is attributed to the deformation-induced nano-twinning as revealed by the TEM measurement. Furthermore, the pronounced dislocation activity and deformation twinning are responsible for the steady work hardening behavior, which postpones the onset of necking instability. It reveals the potential possibility of HIP in additive manufacturing of CrCoNi MEA with the excellent mechanical properties at cryogenic temperature.

Keywords: Medium entropy alloy, CrCoNi, Selective laser melting, Hot isostatic pressing, Cryogenic mechanical properties, Simulation.

TABLE OF CONTENTS

ACKNOWLEDGMENT	1
ABSTRACT	2
TABLE OF CONTENTS	3
LIST OF FIGURES.....	5
LIST OF TABLES.....	7
1. INTRODUCTION.....	8
1.1 Overview of high entropy alloy and medium entropy alloy	8
1.1.1 High entropy alloy.....	8
1.1.2 Medium entropy alloy	9
1.2 Overview of Additive Manufacturing	10
1.3 Overview of Hot Isostatic Pressing.....	12
1.4 Objectives	13
2. METHOD.....	14
2.1 Processing	14
2.2. Finite element model.....	16
2.3. Mechanical testing	17
2.4. Microstructural characterization	17
3. RESULTS AND DISCUSSION	18
3.1. Optimal SLM processing parameters.....	18
3.2. Finite element simulation.....	20
3.3. Phase constituent and microstructure.....	22
3.4 Mechanical properties	24
3.5 Deformation mechanism	29
4. CONCLUSION	35

REFERENCE 37

LIST OF FIGURES

Figure 1.1 Atomic structure model of FCC CoCrFeMnNi [1]	8
Figure 1.2 Seven additive manufacturing processes according to ASTM Committee F42 on Additive Manufacturing [14]	11
Figure 1.3 The selective laser melting (SLM) printing process [21]	12
Figure 2.1 (a) SEM image of CrCoNi powder with EDS analysis result and (b) the corresponding distribution of powder particles used in the SLM process.	14
Figure 2.2 Schematic of the specimen preparation: (a) a laser scanning strategy with a layer-by-layer rotation of the scan direction by 67° in the SLM process, (b) a rectangular bar built on the base plate, and (c) a tensile specimen extracted from the as-built or HIP-treated rectangular bar.	15
Figure 2.3 Finite element model for single track thermal analysis of SLM process of CrCoNi MEA.....	16
Figure 3.1 Window chart of processing parameters correlated to the energy density, relative density and hardness.....	20
Figure 3.2 (a) Cross-sectional macrostructure of the as-built CrCoNi specimen and (b) finite element simulation of melting pool morphology under the optimal processing parameters ($P = 240$ W, $v = 533$ mm/s).....	21
Figure 3.3 Finite element simulation of temperature history during SLM process of CrCoNi MEA.....	22
Figure 3.4 (a) CrCoNi raw powder, (b) as-built CrCoNi MEA-SLM and (c) HIP-treated specimens.	23
Figure 3.5 Dislocation densities estimated from X-ray diffraction peaks in the as-built and HIP	

treated CrCoNi MEA-SLM specimens.	24
Figure 3.6 The undeformed microstructures of as-built (upper) and HIP-treated (lower) CrCoNi MEA-SLM specimens: (a & d) IPF map, (b & e) IQ map, (c & f) KAM map and (g & h) Schmid factor distribution map.	25
Figure 3.7 (a) Engineering stress-strain and (b) work hardening rate curves of as-built and HIP-treated CrCoNi MEA-SLM specimens at room (298 K) and cryogenic (150 K) temperatures.	27
Figure 3.8 Yield strength and elongation of MEAs prepared by different processes: (a) room (298 K) and (b) cryogenic (150 K) temperatures.	28
Figure 3.9 SEM images of fracture surface morphology of as-built and HIP-treated CrCoNi MEA-SLM specimens after tensile test at room (298 K) and cryogenic (150 K) temperatures.	29
Figure 3.10 The IPF, IQ and KAM maps of deformed microstructures of as-built CrCoNi MEA-SLM at an engineering strain of 0.3 at room (298 K) and cryogenic (150 K) temperatures. ..	30
Figure 3.11 The IPF, IQ and KAM maps of deformed microstructures of HIP-treated CrCoNi MEA-SLM at engineering strain of 0.3 at room (298 K) and cryogenic (150 K) temperatures.	31
Figure 3.12 TEM micrographs showing microstructural evolution with strain ($\epsilon = 0.3$) at room (298 K) and cryogenic (150 K) of as-built specimen.	32
Figure 3.13 TEM micrographs showing microstructural evolution with strain ($\epsilon = 0.3$) at room (298 K) and cryogenic (150 K) of HIP-treated specimen.	34

LIST OF TABLES

Table 1 Processing parameters used in the SLM process for fabrication of CrCoNi MEA. ...	18
Table 2. The yield strength (σ_Y), ultimate tensile strength (σ_{UTS}), elongation to fracture (e_f) and hardening capacity (H_c) of as-built and HIP treated CrCoNi MEA-SLM at room (298 K) and cryogenic (150 K) temperatures.	26

1. INTRODUCTION

1.1 Overview of high entropy alloy and medium entropy alloy

1.1.1 High entropy alloy

High entropy alloys (HEAs) are alloys formed by mixing equal or relatively large proportions of (usually) five or more elements. Before these substances were synthesized, typical metal alloys consisted of one or two major components with minor amounts of other elements. For example, additional elements can be added to iron to improve its properties, producing an iron-based alloy, but typically in fairly low percentages, such as the percentages of carbon, manganese, and others in various steels [1]. Hence, high-entropy alloys are a novel class of materials [1, 2]. The term "high-entropy alloys" was coined because the entropy increase of mixing is significantly higher when there is a greater number of elements in the mix, and their percentages are more nearly equal [3].

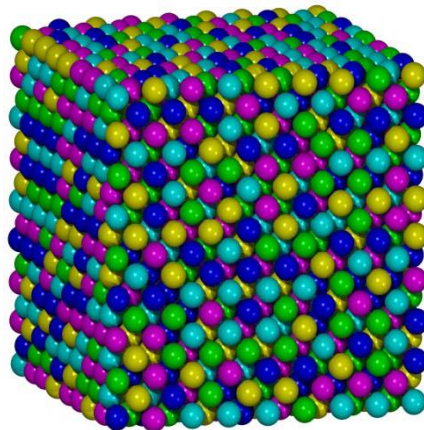


Figure 1.1 Atomic structure model of FCC CoCrFeMnNi [1]

With the ongoing demands of developing advanced structural materials, equiatomic multi-component metallic materials have recently gained enormous attention because of their promising mechanical properties including outstanding combinations of tensile strength, ductility and toughness as well as excellent corrosion and wear resistance [4, 5]. These four

core effects enable HEAs many interesting properties such as outstanding mechanical properties, high specific strength, good corrosion resistance, high radiation resistance etc. Among these, the pure face-centered cubic (FCC) structured CrCoNiFeMn HEA is well-known for its excellent mechanical properties at cryogenic and ambient temperature [6].

1.1.2 Medium entropy alloy

Based on HEAs, the recently developed CrCoNi medium entropy alloy (MEA) has attracted much interest as a promising candidate for advanced structural materials in cryogenic application due to the outstanding strength-ductility combination in addition to excellent fracture toughness [7, 8]. It was reported that the transition from dislocation activity to deformation twinning was the predominant factor for the simultaneously enhanced mechanical properties at cryogenic temperature. Gludovatz et al. [9] addressed that the excellent combination of tensile strength (1.3 GPa), elongation (90%) and fracture toughness ($275 \text{ MPa}\sqrt{m}$) in the CrCoNi MEA at cryogenic temperature (150 K) was attributed to the formation of deformation-induced nano-twinning. Besides the deformation twinning, the FCC (face-centered cubic) to HCP (hexagonal close-packed) phase transition has been reported to be an additional reason for the improved mechanical properties of CrCoNi MEA [10-12]. Recently, Ding et al. [13] performed in situ straining in transmission electron microscopy (TEM) at cryogenic temperature (93 K) to provide an insight into the understanding of the deformation mechanisms of CrCoNi MEA. They found that the coalescence effects of deformation mechanisms, including twinning, the glide of partials and full dislocations, extensive cross-slip, and multiple slips activated by dislocation and grain-boundary interactions were responsible for the exceptional damage tolerance at cryogenic temperature.

Most of the previous studies so far have investigated the CrCoNi MEA produced by the conventional casting-based manufacturing process, which are limited to complex shape and

produce coarse grain materials. In addition, it is difficult to control the microstructure of the casting-based alloys. Some of the deficiencies such as coarse grains and anisotropic solidification microstructures can be formed, thus leading to a significant deterioration in the mechanical properties of the alloy.

1.2 Overview of Additive Manufacturing

The concept of additive manufacturing (AM) dates back to 1945 and the publication of Murray Leinster's short story, 'Things Pass By.' However, this early idea was not really developed until 1971 when Johannes F Gottwald patented the Liquid Metal Recorder, a continuous inkjet metal material device that could form a removable metal fabrication on a reusable surface. This was developed further with Hideo Kodama's invention of 3D printing equipment in 1980, although even then the funding and interest for the technology were limited. Further patents quickly followed, including for the stereolithography process and Bill Masters' Computer Automated Manufacturing Process and System in 1984. 3D printing is a synonym for additive manufacturing, they are two terms for the same process which both mean the same thing. However, 'additive manufacturing' is generally the term used by industry. Additive manufacturing is different from traditional manufacturing as it allows a part to be built layer-by-layer, whereas traditional manufacturing often requires a part to be made by joining separate components or by machining away unwanted material to produce the part. AM is important for the creation of lighter, complex designs that may be too difficult or expensive to produce using traditional manufacturing techniques. Removing the need for molds, milling or machining, AM offers a range of advantages for both prototyping and production. AM technologies can be broadly divided into three types. The first of which is sintering whereby the material is heated without being liquified to create complex high-resolution objects. Direct metal laser sintering uses metal powder whereas selective laser sintering uses a laser on thermoplastic powders so

that the particles stick together. The second AM technology fully melts the materials, this includes direct laser metal sintering which uses a laser to melt layers of metal powder and electron beam melting, which uses electron beams to melt the powders. The third broad type of technology is stereolithography, which uses a process called photopolymerization, whereby an ultraviolet laser is fired into a vat of photopolymer resin to create torque-resistant ceramic parts able to endure extreme temperatures.

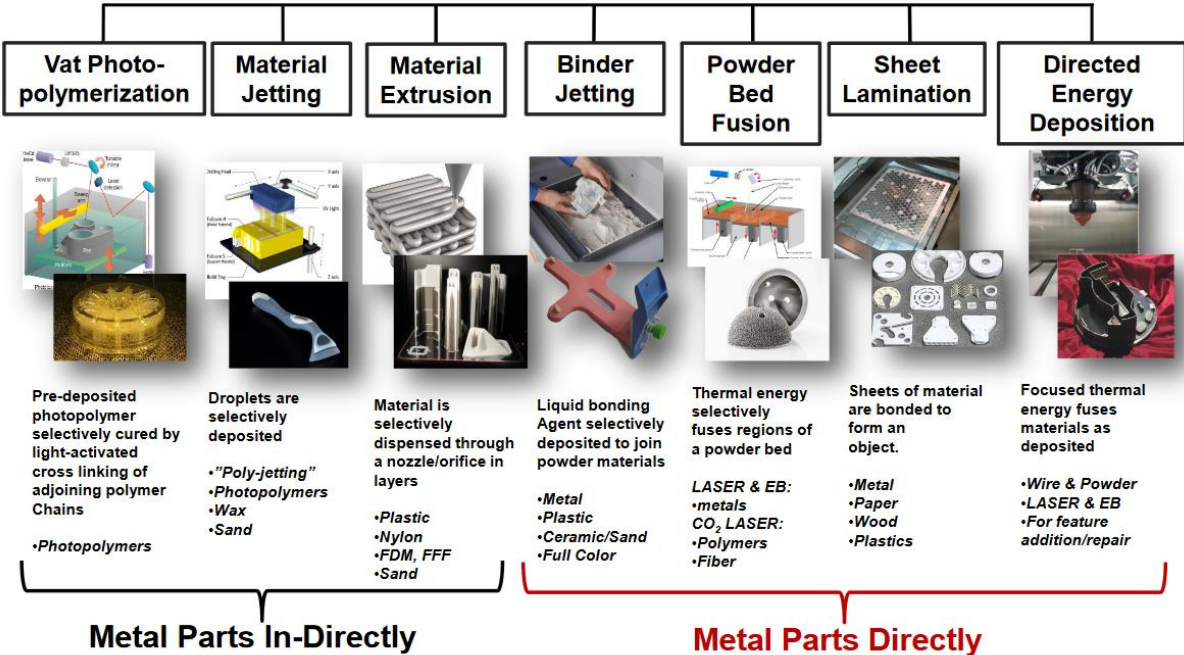


Figure 1.2 Seven additive manufacturing processes according to ASTM Committee F42 on Additive Manufacturing [14]

With the advanced and versatile processing technique, additive manufacturing (AM) has been successfully adopted to fabricate metallic alloys such as Fe-based alloys [15, 16], Ti-based alloys [17, 18], and high entropy alloys (HEAs) [19, 20]. During the AM process, the rapid solidification rate and high-temperature gradients of the melting pool can result in the homogeneous solid solution microstructure and grain refinement of the AM parts. Selective laser melting (SLM) is one of the representative AM techniques that use layer build-up technology to produce high-quality, complex geometries by melting metallic powders with a high-power laser.

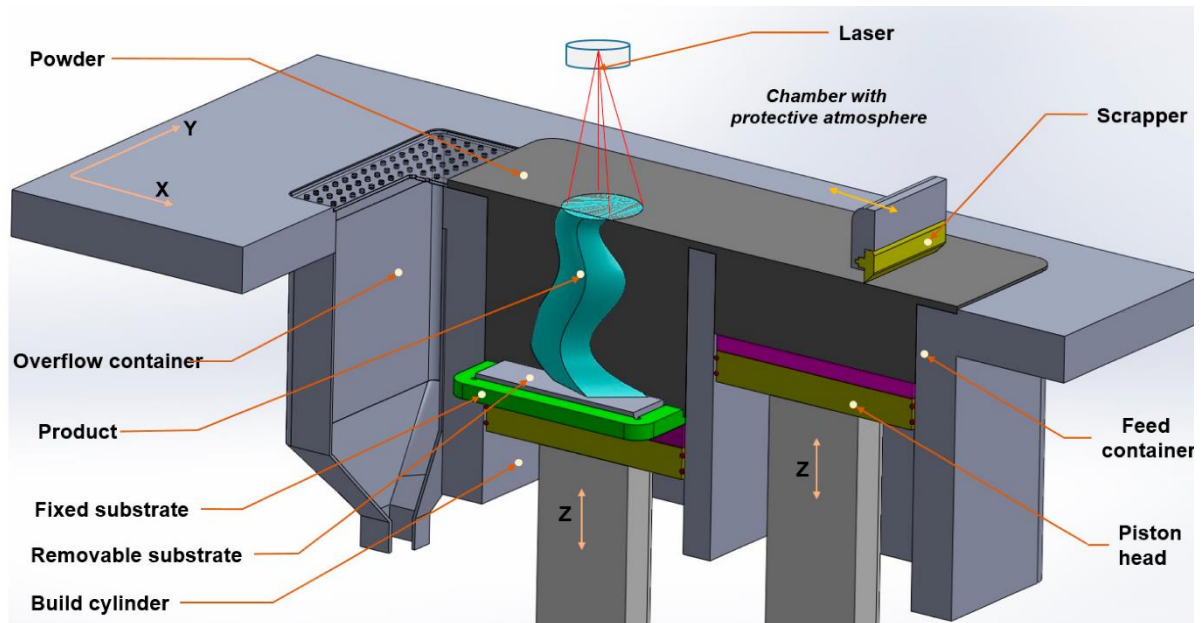


Figure 1.3 The selective laser melting (SLM) printing process [21]

Up to now, there have been few reports on the utilization of AM to comprehensively investigate the microstructure and mechanical properties of CrCoNi MEA. Zhang et al. [22] studied the corrosion behavior of SLM CrCoNi MEA and provided a comprehensive comparison to the casting MEA. Han et al. [23] showed that the CrCoNi MEA fabricated by SLM revealed a high ultimate tensile strength of 1.3 GPa and elongation of 47% with the hierarchical microstructure at cryogenic temperature (150 K) due to the enhanced dislocation and nano-twinning behaviors.

1.3 Overview of Hot Isostatic Pressing

Hot isostatic pressing (HIP) is a manufacturing process, used to reduce the porosity of metals and increase the density of many materials. This improves the material's properties and workability. The post-processing treatment of hot isostatic pressing (HIP) has been used in AM components due to the positive influence on the mechanical properties and microstructure [24, 25]. In the HIP process, the alloys are subjected to high temperature and softened under the high isostatic pressure in order to reduce the size and the number of pores. The literature reports

that the significant reduction of metallurgical defects such as pores, voids or lack of fusion after HIP resulted in the improved densification and tensile strength in the Ti-based alloys [17, 18], Ni-based alloys [26, 27], Fe-based alloys [15, 16] and HEAs [19, 20]. To the best of the author's knowledge, there have been no efforts to investigate the effect of HIP on the microstructure and tensile properties of SLM CrCoNi MEA at cryogenic temperature.

1.4 Objectives

CrCoNi MEA powder was picked up to:

- Fabricate under the optimal processing via 3D printing SLM process.
- Cryogenic elastoplastic deformation properties evaluation and deformation mechanism according to operating temperature.
- Evaluation of fracture mechanics properties at room and cryogenic temperatures and identification of fracture mechanisms.

2. METHOD

2.1 Processing

The starting material was the CrCoNi MEA powder with a weight ratio of 33.65% Cr, 33.19% Co, 33.16% Ni, which was confirmed by the energy dispersive spectroscopy (EDS) analysis result as shown in Fig. 2.1. The CrCoNi MEA powder has a spherical shape (Fig. 2.1(a)) with an average particle size of 33 μm (Fig. 2.1(b)). Cubic blocks of $7 \times 7 \times 7 \text{ mm}^3$ in size were produced with various laser power and scanning speed, using constant scanning strategy with 67° rotation of successive layer to evaluate the density and micro-hardness, and the optimal SLM processing condition were determined based on the density. After cutting, the cross-section surface of the cubic block was observed by optical microscopy. The density of block specimens was assessed by the ratio of pore area to cross-section area. In order to obtain the hardness variation of block specimens under different process parameters, the micro-hardness test was carried out using NMT-X3 micro-hardness tester with a load of 300 g and a dwelling time of 15 s.

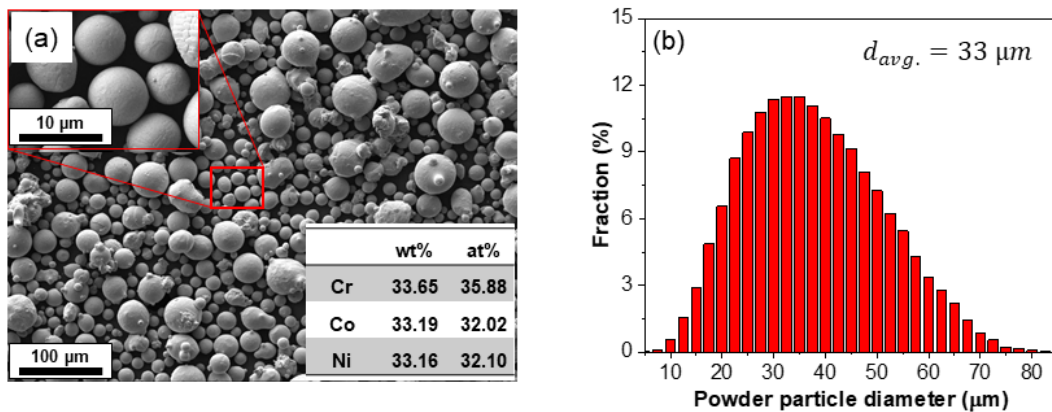


Figure 2.1 (a) SEM image of CrCoNi powder with EDS analysis result and (b) the corresponding distribution of powder particles used in the SLM process.

And then, rectangular bars of $12 \times 12 \times 97 \text{ mm}^3$ in size were produced using the optimal processing condition. A schematic of the specimen preparation by SLM process is provided in

Fig. 2.2(a) and tensile specimens were extracted from the rectangular bar as shown in Fig. 2.2(b, c). Argon gas was used as shielding gas during the SLM process. To investigate the effect of process parameters on the fabrication quality of specimens, different process parameters were selected, as listed in Table 1. The energy density (E) used for evaluating the fabrication quality of block specimen is calculated using Eq. (1) [28, 29].

$$E = \frac{P}{h \times v \times t} \quad (1)$$

where P is the laser power, h is the hatch space, v is the scanning speed and t is the layer thickness.

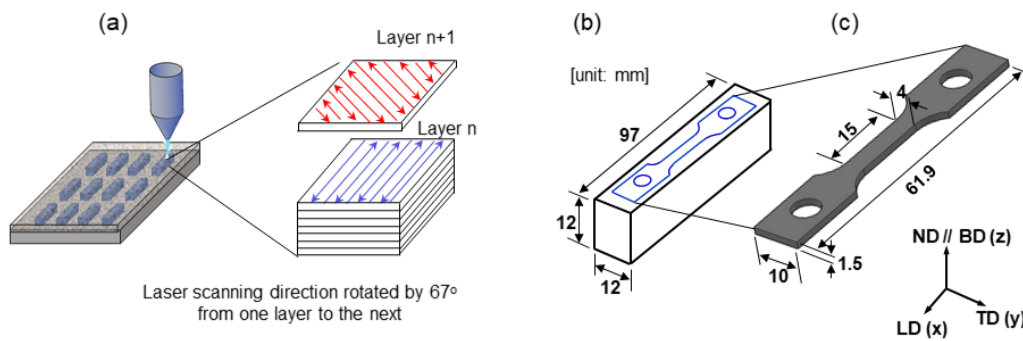


Figure 2.2 Schematic of the specimen preparation: (a) a laser scanning strategy with a layer-by layer rotation of the scan direction by 67° in the SLM process, (b) a rectangular bar built on the base plate, and (c) a tensile specimen extracted from the as-built or HIP-treated rectangular bar.

After the SLM process under the optimal processing condition, the as-built specimens were subjected to hot isostatic pressing (HIP) treatment for improving the alloy densification by close pores or eliminating metallurgical defects [30]. In the HIP treatment, the as-built rectangular specimens were subject to the isostatic pressure of 1000 atm in high purity Argon gas atmosphere at the elevated temperature of 1150°C with and holding time of 4 h, and then cooled to room temperature in the furnace.

2.2. Finite element model

The optimal process parameters were used in the finite element thermal analysis of a single track based on the heat conduction model to obtain the melting pool size and temperature history during the SLM process. The thermal physical properties of CrCoNi MEA were defined through a numerical model based on thermodynamic calculations using JmatPro and calibrated by the experimental data at room temperature. Considering the phase change during the SLM process, some thermal material properties of powder were determined by the porosity and bulk material properties.

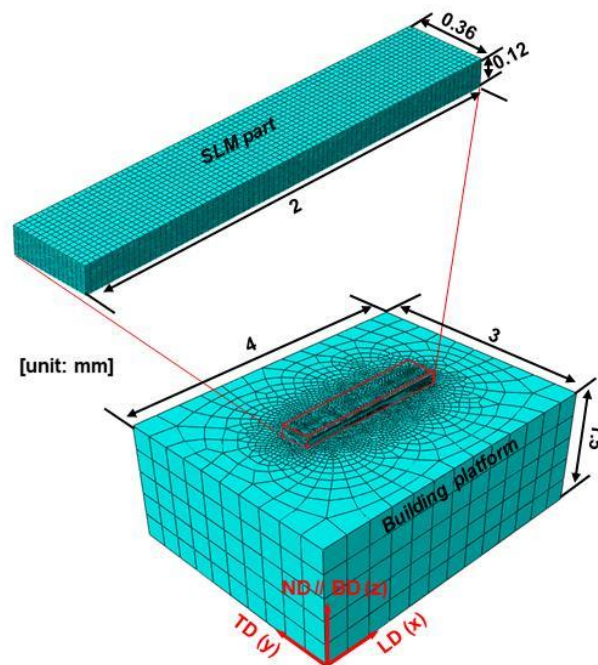


Figure 2.3 Finite element model for single track thermal analysis of SLM process of CrCoNi MEA.

The finite element model is shown in Fig. 2.3. The size of the mesh element in deposition layers was $25 \times 22 \times 8 \mu\text{m}^3$. The use of fine mesh around a large temperature gradient could ensure the accuracy of thermal analysis. And the element size of the building platform was $300 \times 300 \times 300 \mu\text{m}^3$ to reduce the computational cost. In the thermal analysis, the laser energy modeled by the double ellipsoidal model was adjusted to generate the morphology of the melting pool in order to compare it with the result of the cross-sectional macrostructure. And

the heat convection and radiation were applied to the surface of the model without the bottom of the platform to consider the heat loss.

2.3. Mechanical testing

The mechanical tests of as-build and HIP treated CrCoNi MEA-SLM specimens were performed using a Zwick Roell Xforce Z100 universal machine at an engineering strain rate of 10^{-3} s^{-1} under room (293 K) and cryogenic (150 K) temperatures. Tensile tests were either carried out until fracture or interrupted at an engineering strain of 0.3. The tensile test at 150 K was conducted in a cryogenic chamber with the temperature controller. An extensometer was used to measure the strain during the tensile tests.

2.4. Microstructural characterization

X-ray diffraction (XRD) analysis was employed with Cu K_{α} radiation of $\lambda = 0.154 \text{ nm}$; 2θ ranging from 20° to 100° ; step width of 0.02° and scan speed of $5^{\circ}/\text{min}$ to characterize phases of CrCoNi raw powder, as-build and HIP treated specimens. The microstructure was characterized via FE-SEM equipped with electron backscatter diffraction (EBSD); inverse pole figure (IPF), image quality (IQ) and kernel average misorientation (KAM) maps were compiled. A transmission electron microscope (TEM) was employed to characterize microstructure and deformation mechanism. Mechanical grinding and polishing were performed to prepare TEM specimens with 3 mm diameter, which were ground on SiC paper and diamond abrasives on both sides until the thickness was approximately $100 \mu\text{m}$. Then, the specimen was dimpled using a Gatan Model 656 Dimple grinder. The final thinning was applied using a Gatan Model 691 PIPS (Precision Ion Polishing System) instrument. Metallographic observations were conducted utilizing a high-resolution transmission electron microscopy (HRTEM, JEOL-2100F). By using the JEOL 2100F, selected area electron diffraction (SAED) patterns of the samples were also obtained.

3. RESULTS AND DISCUSSION

3.1. Optimal SLM processing parameters

Prior to investigating the mechanical properties of SLM CrCoNi MEA, the optimal processing parameters used in the SLM process for fabrication of CrCoNi MEA specimens were determined. As listed in Table 1, a total of 48 processing parameters were adopted to obtain the surface morphology characterized by the relative density which was used to evaluate the optimization of processing parameters such as scanning speed (v) and laser power (P). The energy density and micro-hardness were also achieved for a comprehensive comparison as depicted in Fig. 3.1.

Fig. 3.1 shows that the surface morphology of SLM block specimens significantly varies with the processing parameters. Regardless of the laser power, the surface morphology exhibits an extensive porosity with the low relative density (81.98%) at the high scanning speed ($>1,300$ mm/s). As the scanning speed decreases ($<1,000$ mm/s), however it reveals the improved surface morphology with the high relative density ($>99.5\%$). Fig. 3.1 reveals that the good surface morphology with the highest relative density of 99.97% was observed at the scanning speed of 533 mm/s and laser power of 240 W, which is determined as the optimal processing parameters for fabrication of CrCoNi MEA specimens in the present study.

Table 1 Processing parameters used in the SLM process for fabrication of CrCoNi MEA.

Process parameters	Value
Layer thickness (μm)	30
Hatch spacing (μm)	90
Beam size (μm)	100
Laser power (W)	160; 200; 240; 280; 320; 360
Scanning speed (mm/s)	399; 533; 667; 889; 1,111; 1,333; 1,556; 1,778

Furthermore, the correlation between processing parameters with the energy density,

relative density and micro-hardness are discussed. At constant laser power, the energy input decreases with the increase of scanning speed. Insufficient energy input causes the formation of defects such as unmelt powder, pores in the block specimen. In addition, the key-hole defects can form when pockets of gas become trapped into the melting layers at high laser power and low scanning speed. Such defects can potentially lead to a decrease in density. As shown in Fig. 4, the relative density decreases from $99.70 \pm 0.32\%$ to $87.23 \pm 5.45\%$ as the scanning speed increases from 399 mm/s to 1,778 mm/s. However, the relative density also can be decreased as the scanning speed is low (~ 200 mm/s [31]). The effect of laser power on the density becomes attenuated as the scanning speed decreases. In specific, with the lowest scanning speed of 399 mm/s, the effect of laser power on the density is almost negligible with a standard deviation within 0.32%, while it increases noticeably to 5.45% at the highest scanning speed of 1,778 mm/s

At constant scanning speed, the density of the block specimens increases as the laser power increases. At high scanning speed, the input energy is inadequate and the spreading of the liquid metal is weakened, resulting in deterioration of the surface quality of block specimen. A balling defect occurred because the single track became discontinuous, and some unmelted powders were observed at the boundary of the single track. On the other hand, at low scanning speed, the solidification time of the melt pool is prolonged and the liquid metal has a longer time to spread out, therefore, the single track spreads well and is continuous. The effect of scanning speed on the density of the block specimen becomes more sensitive as the laser power decreases. With a laser power of 360 W, the effect of scanning speed on the density of block specimen is negligible with a standard deviation within 0.53%, while the block specimen with 160 W laser power shows a high standard deviation up to 6.03%. Accordingly, the relative density increases from $95.27 \pm 6.03\%$ to $99.55 \pm 0.53\%$ as the laser power decreases from 360 W to 160 W.

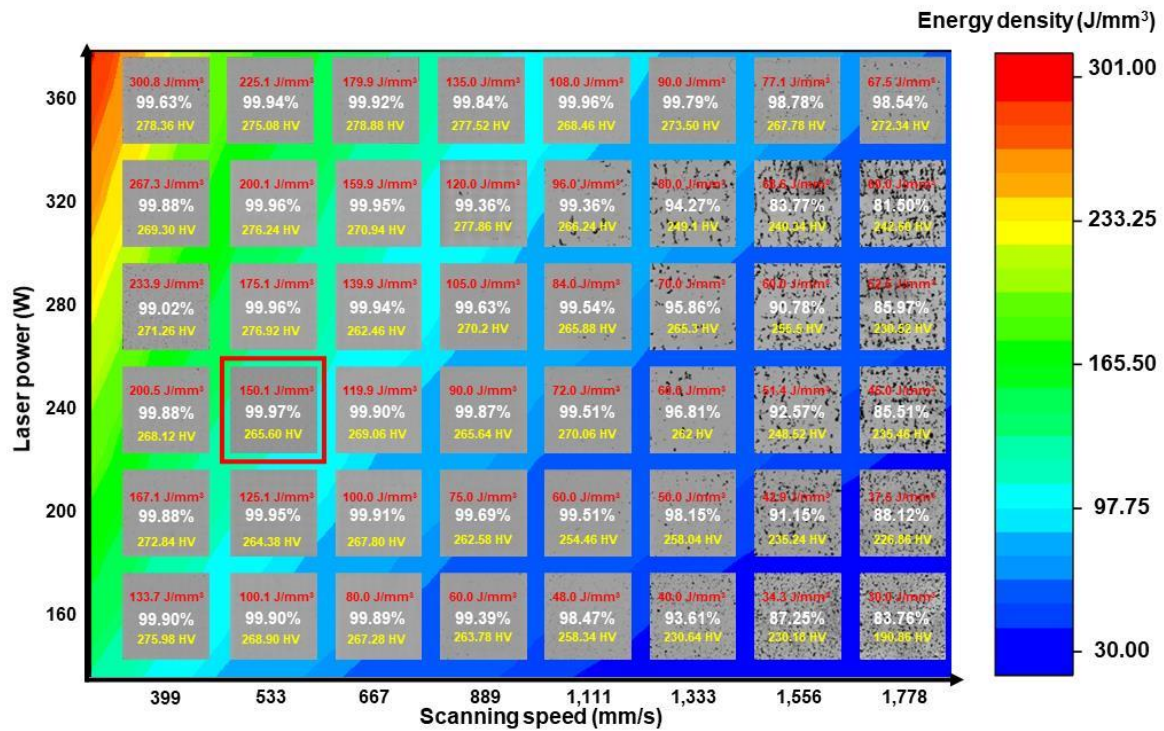


Figure 3.1 Window chart of processing parameters correlated to the energy density, relative density and hardness.

The energy density of block specimen ranges from 30.0 to 300.8 J/mm³. As shown in Fig. 3.1, the maximum relative density reaches to 99.97% at the energy density of 150.1 J/mm³ ($v = 240$ W and $P = 533$ mm/s). Moreover, at the lowest energy density of 30.0 J/mm³, the minimum micro-hardness (HV₃₀) of 190.86 HV is obtained. It reveals that the micro-hardness increases as the energy density increases. However, there is a little change when the energy density exceeds 180 J/mm³ at which the micro-hardness reaches the maximum of 278.88 HV.

3.2. Finite element simulation

Fig. 3.2 shows the cross-sectional macrostructure of the as-built CrCoNi specimen measured by optical microscope and finite element simulation of melting pool morphology under the optimal processing parameters ($P = 240$ W, $v = 533$ mm/s). Fig. 3.2(a) shows that the melting pool morphology and laser scanning strategy with 67° rotation of successive layers

during the SLM process are well revealed. As shown in Fig. 3.2(a), the measured melting pool depth and width are 46 μm and 202 μm , respectively. While Fig. 3.2(b) reveals similar results obtained by the FE simulation to be 42 μm and 198 μm for the melting pool depth and width, respectively. It is noted that the FE simulation was conducted using the single track, therefore, the laser scanning strategy with 67° rotation is not shown here. The simulation result shows that the morphology and size of the melting pool agree well with the experiment.

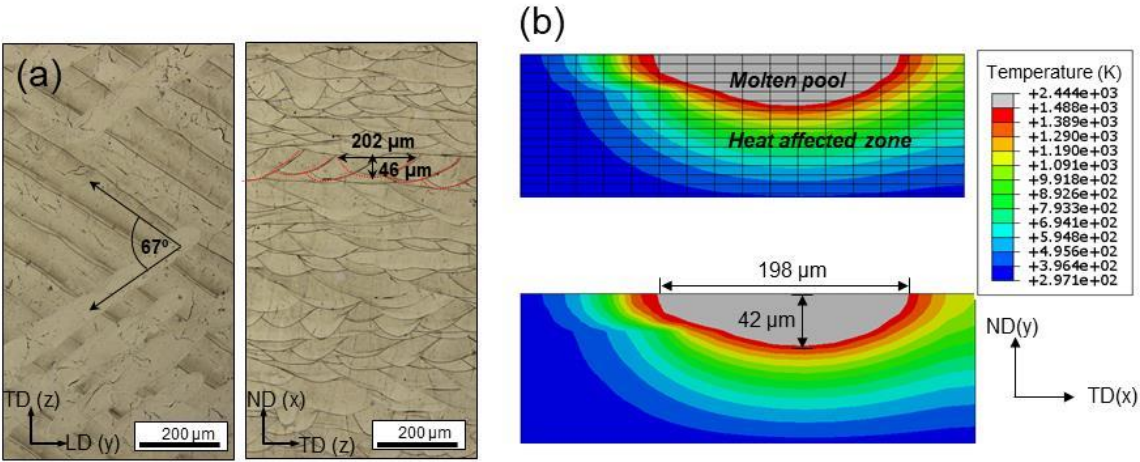


Figure 3.2 (a) Cross-sectional macrostructure of the as-built CrCoNi specimen and (b) finite element simulation of melting pool morphology under the optimal processing parameters ($P = 240 \text{ W}$, $v = 533 \text{ mm/s}$)

In the SLM process, high energy input is provided into a large material at almost room temperature. That can rapidly absorb heat from a high-temperature region. This implies that when the metal reaches the maximum temperature in the SLM process, it is capable of reaching a high cooling rate ($3.2 \times 10^6 \text{ K/s}$). Indeed, the phenomenon is observable in the simulation as plotted in Fig. 3.3. The high cooling rate may result in the fine microstructure and high dislocation density of SLM part. It will be discussed further in the following section.

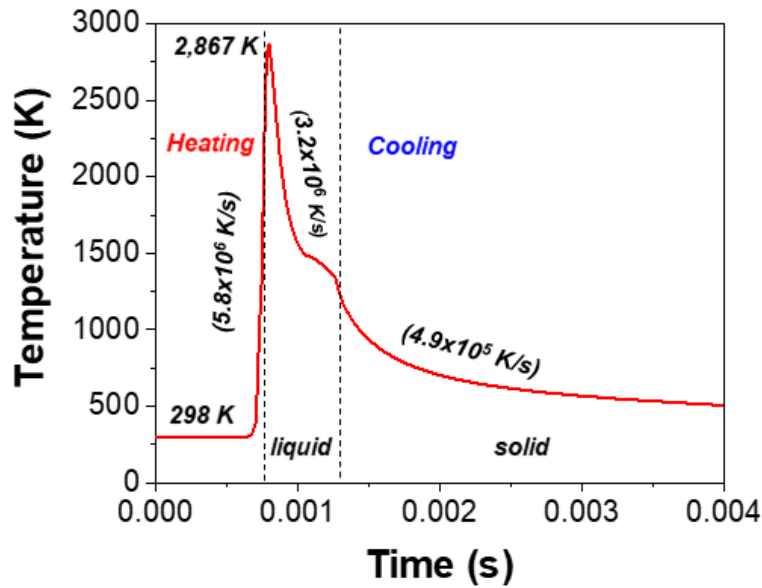


Figure 3.3 Finite element simulation of temperature history during SLM process of CrCoNi MEA.

3.3. Phase constituent and microstructure

Fig. 3.4 shows the XRD analysis results of the raw powders, as-built and HIP treated CrCoNi MEA specimens. It is obvious that only a single face-centered cubic (FCC) phase was detected for the CrCoNi MEA and no phase transformation takes place during the SLM process and after HIP treatment. Similar diffraction peaks with a little change in intensity are observed. The initial dislocation density of different diffraction peaks was estimated from XRD analysis results following a previous study [30] and plotted in Fig. 3.5. As shown in Fig. 3.5, the initial dislocation density of different diffraction peaks in the as-built CrCoNi MEA-SLM decreases after HIP. The higher initial dislocation density in the as-built specimen can increase the dislocation strengthening, consequently leading to the higher strength which will be confirmed in Section 3.4

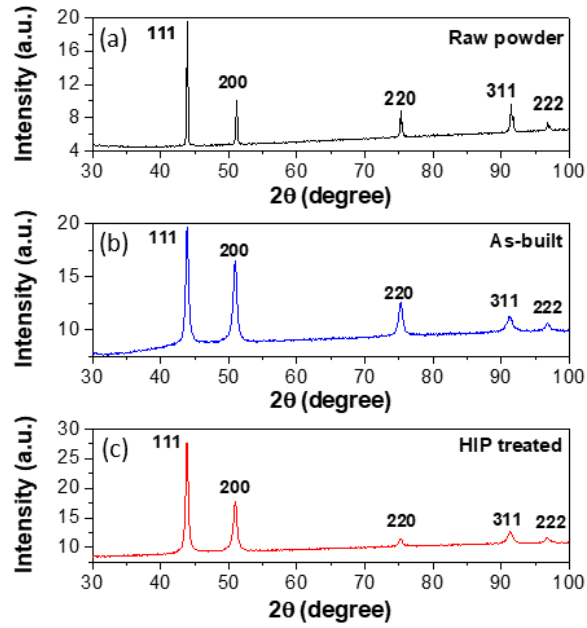


Figure 3.4 (a) CrCoNi raw powder, (b) as-built CrCoNi MEA-SLM and (c) HIP-treated specimens.

Fig. 3.6 shows the undeformed microstructures of as-built and HIP-treated CrCoNi SLMMEA specimens. As shown in Fig. 3.6(a), the grain structure of the specimen after SLM mainly consists of the columnar elongated along the building direction. The average grain size of the as-built specimen was estimated to be $54.24 \pm 9.00 \mu\text{m}$. In Fig. 3.6(d), the grain structure of HIP treated specimen is dominated by equiaxed morphology with an average grain size of $45.76 \pm 9.32 \mu\text{m}$. It should be noted that the average grain size of as-built and HIP treated CrCoNi MEA-SLM was determined by including the twin boundaries. Fig. 3.6(b) shows that the as-built one reveals a lot of low angle grain boundaries (LAGBs) in a grain enclosed by high angle grain boundaries (HAGBs) while the HIP treated specimen exhibits a significant amount of annealing twins with the boundary in green, as shown in Fig. 3.6(e).

For the as-built CrCoNi MEA-SLM, the high cooling rate of $3.2 \times 10^6 \text{ K/s}$ during the SLM process leads to an increase in dislocation density and residual stress, hence a high yield strength [30]. Initial dislocations or stacking faults are indicated in the high KAM region [30].

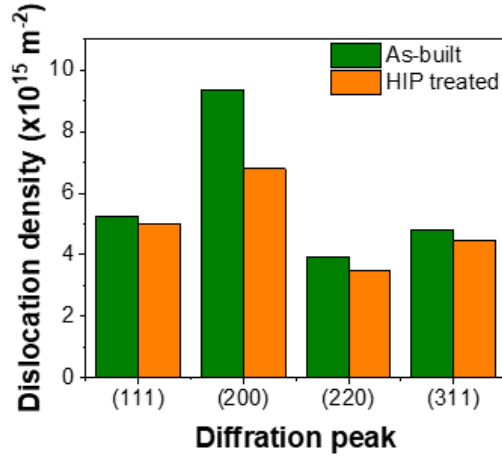


Figure 3.5 Dislocation densities estimated from X-ray diffraction peaks in the as-built and HIP treated CrCoNi MEA-SLM specimens.

In Fig. 3.6(c), the as-built CrCoNi MEA-SLM shows a more heterogeneous KAM distribution and a more significant intragranular orientation spread than the HIP treated one as shown in Fig. 3.6(f). In contrast, the HIP treated was characterized by low average local misorientation angles (in blue), implying the annihilation of initial dislocation and relaxation of inner residual stresses during the HIP treatment at 1150 °C. Fig. 3.6(g, h) shows a similar distribution of Schmid factor in the undeformed microstructures of the as-built and HIP-treated specimens. It reveals that most grains have a high value of the Schmid factor represented by the red color as shown in Fig. 3.6(g, h).

3.4 Mechanical properties

Fig. 3.7 shows the mechanical properties of SLM CrCoNi MEA at room (298 K) and cryogenic (150 K) temperatures. Note that the tensile test results were obtained using the CrCoNi MEA specimens fabricated by SLM process with the optimal processing parameters as discussed in Section 3.1. The ultimate tensile strength (σ_{UTS}), yield strength (σ_Y), elongation to fracture (e_f) and hardening capacity (H_C) are summarized in Table. 2. Note that the H_C is calculated for the strain hardening behavior using the equation, $H_C = (\sigma_{UTS} - \sigma_Y)/\sigma_Y$.

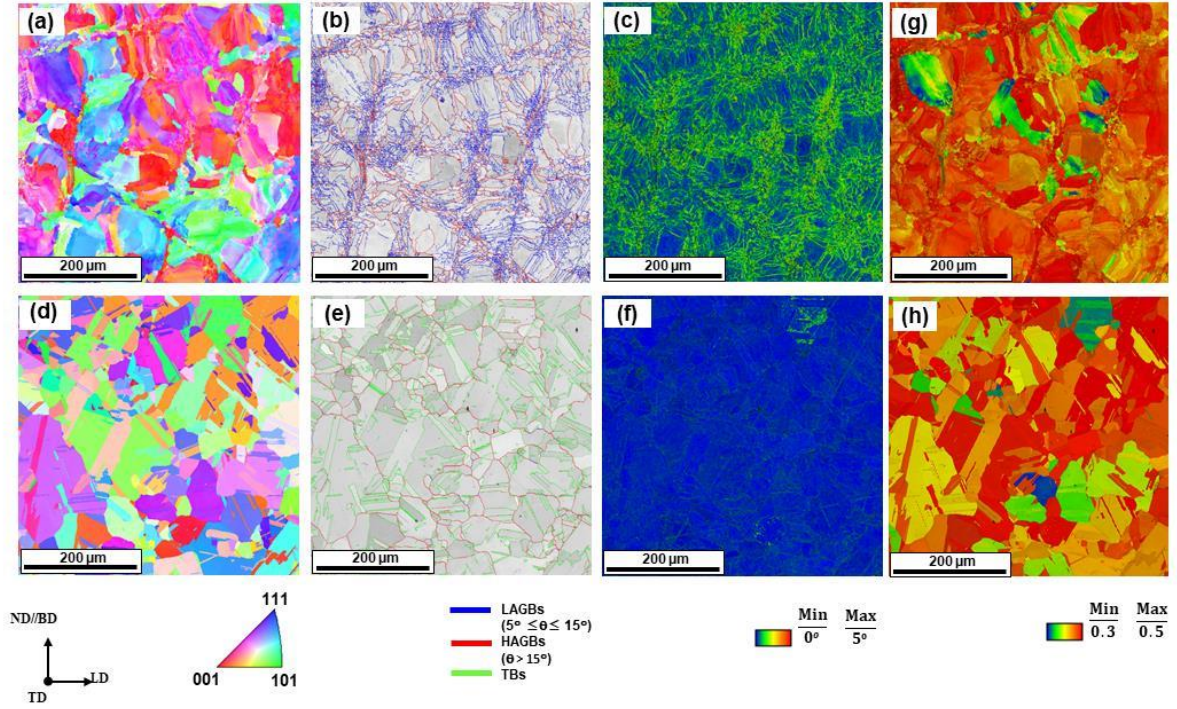


Figure 3.6 The undeformed microstructures of as-built (upper) and HIP-treated (lower) CrCoNi MEA-SLM specimens: (a & d) IPF map, (b & e) IQ map, (c & f) KAM map and (g & h) Schmid factor distribution map.

Fig. 3.7(a) shows the engineering stress-strain curves of as-built and HIP-treated CrCoNi MEA-SLM at room (298 K) and cryogenic (150 K) temperatures. At room temperature, the asbuilt specimens exhibit the σ_{UTS} , σ_Y and e_f of 887 MPa, 695 MPa, and 40%, respectively. After the HIP process, the elongation to fracture is significantly improved by 1.9 times ($e_f = 76\%$) while σ_{UTS} and σ_Y are decreased to 783 MPa and 330 MPa, respectively. The decrease in strength after the HIP treatment can be attributed to the decrease of initial dislocation density as aforementioned. Furthermore, an annihilation of the dislocations due to recrystallization in the HIP treatment can contribute to the decrease in strength of the HIP-treated specimen.

At cryogenic temperature, similar to the single-phase HEAs [7, 32], the mechanical behavior of the CrCoNi MEA-SLM also exhibits a strong temperature dependence. It should be noted that both strength, elongation and hardening capacity of SLM CrCoNi MEA increases as the temperature decreases from 298 K to 150 K. For the as-built specimen, the σ_Y , e_f and H_c

increase from 695 to 740 MPa, from 40 to 44% and from 0.28 to 0.37, respectively. For the HIP-treated one, σ_Y , e_f and H_C increase from 330 to 405 MPa, from 76 to 81% and 0.4 to 1.26, respectively. It also reveals that the as-built CrCoNi SLM-MEA shows a higher strength but lower elongation to fracture than those of HIP-treated one at 150 K.

Table 2. The yield strength (σ_Y), ultimate tensile strength (σ_{UTS}), elongation to fracture (e_f) and hardening capacity (H_C) of as-built and HIP treated CrCoNi MEA-SLM at room (298 K) and cryogenic (150 K) temperatures.

	w/ & w/o HIP	σ_Y [MPa]	σ_{UTS} [MPa]	e_f [%]	H_C
Room Temp.	As-built	695	887	40	0.28
	HIP-treated	330	783	76	0.37
Cryogenic Temp.	As-built	740	1,037	44	0.40
	HIP-treated	405	916	84	1.26

Fig. 3.7(b) presents the work-hardening behavior (the derivative of true stress with respect to true strain, $d\sigma_T/d\varepsilon_T$) of the as-built and HIP-treated CrCoNi MEA-SLM as a function of the true stress. The light blue area indicates the region in which necking is predicted to occur according to Considere's criterion: $d\sigma/d\varepsilon < \sigma$. At 150 K, the work-hardening rate (WHR) of both as-built and HIP-treated specimens is consistently higher than at 298 K and its intersection with the necking line ($d\sigma/d\varepsilon = \sigma$) occurs at higher strain. As a result of the postponement of necking, the elongation at 150 K is higher than at 298 K. The extended region of work-hardening at 150 K compared to 298 K is due to the early onset of twins [8]. At both 298 K and 150 K, all WHR curves can be distinguished into three stages (Fig. 3.7(b)) with an initial rapid decrease followed by a slower second stage and a steep decrease until fracture in the third stage. However, the WHR of HIP-treated one in the second stage is more stable than the as-built CrCoNi MEA-SLM, this behavior is attributed to the primary twinning. Such a similar behavior was also found in the Al0.5CoCrFeMnNi HEA after annealing heat treatment at 1200 °C [33]. In addition, the HIP-treated CrCoNi MEA shows the necking strains of 0.56 and 0.60, which are higher than those of 0.33 and 0.37 for the as-built specimens at 298 K and 150 K,

respectively. This implies the higher elongation to fracture of HIP-treated CrCoNi MEA-SLM compared to the as-built one at both room (298 K) and cryogenic (150 K) temperatures as shown in Fig. 3.7(b).

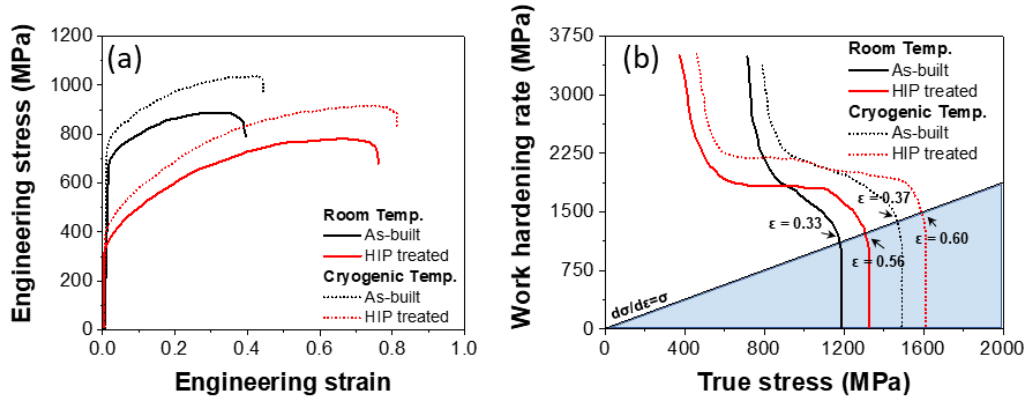


Figure 3.7 (a) Engineering stress-strain and (b) work hardening rate curves of as-built and HIP-treated CrCoNi MEA-SLM specimens at room (298 K) and cryogenic (150 K) temperatures.

Fig. 3.8 shows a comprehensive comparison of yield strength and elongation to fracture of various materials fabricated by different processes at room (298 K) and cryogenic (150 K) temperatures [4, 7, 22, 23, 30, 34-39]. At room temperature, the yield strength and elongation to fracture of as-built (σ_Y : 695 MPa, e_f : 40%) and HIP-treated CrCoNi MEA-SLM (σ_Y : 330 MPa, e_f : 76%) in the present study are comparable to those of MEAs processed by additive manufacturing processes: selective laser melting (SLM) (σ_Y : 651 MPa, e_f : 35.8%) [23], directed energy deposition (DED) (σ_Y : 300-620 MPa, e_f : 35.5-73.0%) [30, 36, 39], laser powder bed fusion (L-PBF) (σ_Y : 551 MPa, e_f : 51.4%) [38]. Compared with the recent study with the same CrCoNi MEA processed by the SLM [23], the as-built CrCoNi MEA-SLM in the present study possesses both greater yield strength and elongation to fracture. In addition, the present study shows a significantly improved elongation to fracture of as-built (e_f : 40%) and HIP-treated (e_f : 76%) CrCoNi SLM-MEA compared to those of other MEAs prepared by casting-based (e_f : 15-44%) [7, 34, 37], mechanical alloying + spark plasma sintering (MA+SPS) (e_f : 25.9%) [35]

processes. At cryogenic (150 K) temperature, as shown in Fig. 3.8(b), the as-built CrCoNi MEA-SLM exposes higher yield strength but lower elongation to fracture compared to the other casting-based MEAs (σ_Y : 447-580 MPa, e_f : 40.5-66.0%) [4, 7, 37]. While the HIP-treated CrCoNi MEA-SLM shows superior elongation. As reported in the previous study [30], the excellent elongation to fracture in the HIP-treated CrCoNi MEA is mainly attributed to the significant reduction of micropores after HIP treatment. In comparison with Fig. 3.8(a, b) shows simultaneous increases of both strength and elongation at cryogenic temperature.

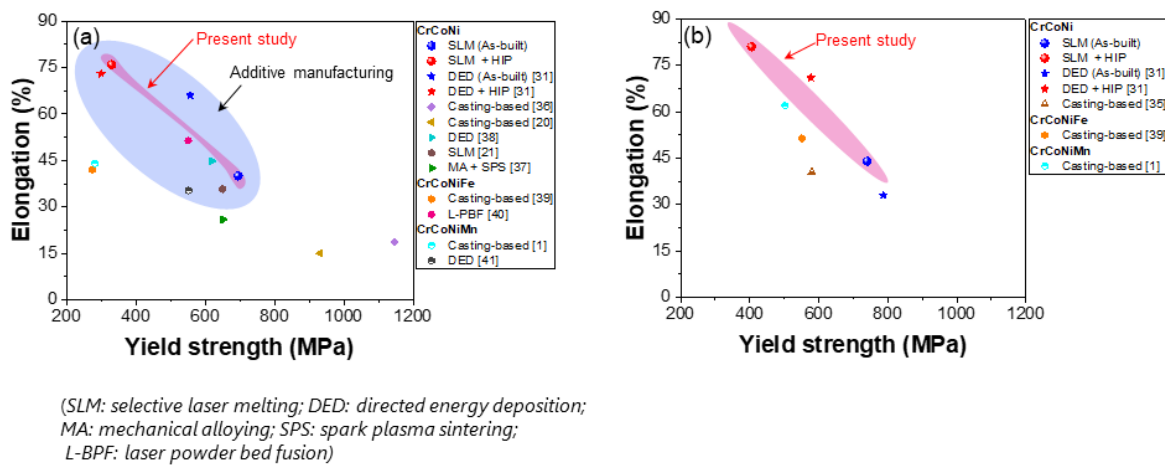


Figure 3.8 Yield strength and elongation of MEAs prepared by different processes: (a) room (298 K) and (b) cryogenic (150 K) temperatures.

As shown in Fig. 3.9, the fractography of as-built and HIP-treated CrCoNi MEA-SLM specimens is characterized by ductile fracture, which is occupied by dimples at both room (298 K) and cryogenic (150 K) temperatures. The HIP-treated specimen shows a more uniform distribution of the dimples with a higher density than the as-built specimen. In addition, pores are not observed in the HIP-treated specimen. As a result, the HIP-treated specimen exhibits a greater elongation to fracture than the as-built one. When considering the effect of temperature, at cryogenic (150 K) temperature, the dimples are smaller and deeper than those at room (298 K) temperature in both as-built and HIP-treated specimens, leading to the increased elongation in both as-built and HIP treated specimens.

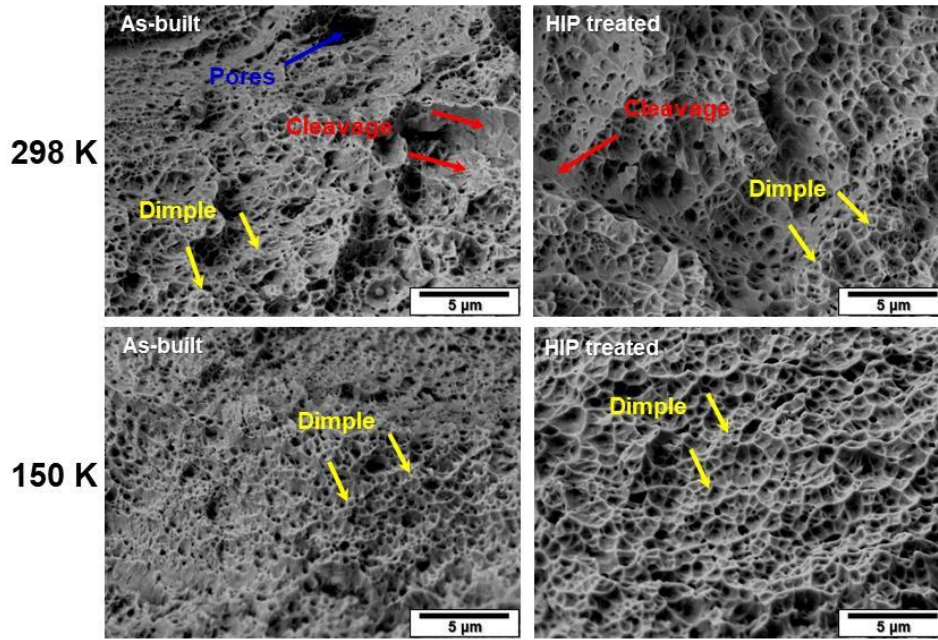


Figure 3.9 SEM images of fracture surface morphology of as-built and HIP-treated CrCoNi MEA-SLM specimens after tensile test at room (298 K) and cryogenic (150 K) temperatures.

3.5 Deformation mechanism

The deformed microstructures of as-built and HIP treated CrCoNi MEA-SLM were characterized at an engineering strain of 30% at room (298 K) and cryogenic (150 K) temperatures, as shown in Figs. 3.10 and 3.11. The IPF maps in Figs. 3.10 and 3.11 show that the formation of $\langle 111 \rangle$ fiber texture is typically observed in the FCC materials [40]. During the tensile deformation, plastic slip occurs firstly in the grains which have a higher Schmid factor as shown in Fig. 3.6 (g, h). Plastic slip leads to the increase of dislocations that are piled up at the grain boundaries, resulting in an increase in the flow stress during deformation. And then plastic slip occurs in more grains under higher flow stress with more slip systems being activated. Along with the plastic deformation, the grains are subject to rotation in order to accommodate the macroscopic plastic deformation, resulting in the deformation texture. However, until the slip plane $\{111\}$ is perpendicular to the tensile axis and the Schmid factor is near zero, slip is hard to continue for the grains with $\langle 111 \rangle$ fiber texture. In this case, further

plastic deformation can be accommodated by deformation twinning [36].

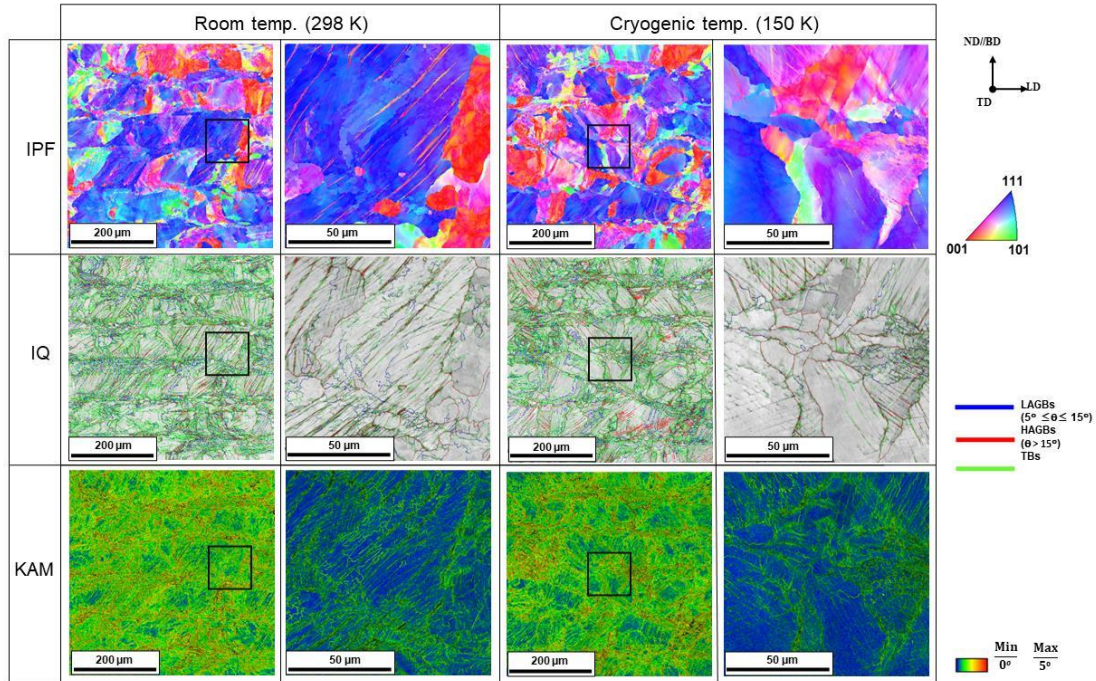


Figure 3.10 The IPF, IQ and KAM maps of deformed microstructures of as-built CrCoNi MEA-SLM at an engineering strain of 0.3 at room (298 K) and cryogenic (150 K) temperatures.

At 298 K, as shown in the enlarged microstructure in the IQ maps in Figs. 3.10 and 3.11, the as-built CrCoNi MEA shows the deformation twinning, while the HIP-treated CrCoNi MEA exposes the synthesis of annealing twins and the formation of deformation twinning. Due to the low stacking fault energy of CrCoNi MEA ($22 \pm 4 \text{ mJ/m}^2$) [8], deformation twins can be activated under room temperature as a supplementary or even a dominant deformation mechanism other than dislocation gliding, leading to enhanced strength and elongation to fracture. In order to elucidate this, the critical stress for twinning is obtained by following the procedure in Ref. [30]. The critical twinning stresses are 312 MPa (as-built) and 322 MPa (HIP-treated), which are lower than the maximum flow stress, implying that the deformation twinning can be readily activated. In addition, the critical twinning for stress in the present study is lower than in the previous study (793–804 MPa) [23], responsible for a greater elongation as shown in Fig. 3.8.

At 150 K, the earlier activation of deformation twinning is also observed in both the deformed microstructures of as-built and HIP-treated CrCoNi MEA, which can become the obstacle to prevent the dislocation movement and consequently results in the continuous accumulation of dislocations at the boundaries of twins and sub-grains. According to the previous reports [8, 41-43], the high cooling and solidification rates lead to an increase in the dislocation density which could be further intensified with the increasing deformations at low temperature. In addition, the interaction between dislocations and twinning also contributed to the increase in dislocation density [42, 44]. Thus, the interaction mechanism of dislocations and deformation twinning results in the increased yield strength and elongation to fracture simultaneously as well as high work-hardening behavior in the as-built and HIP-treated CrCoNi MEA at 150 K.

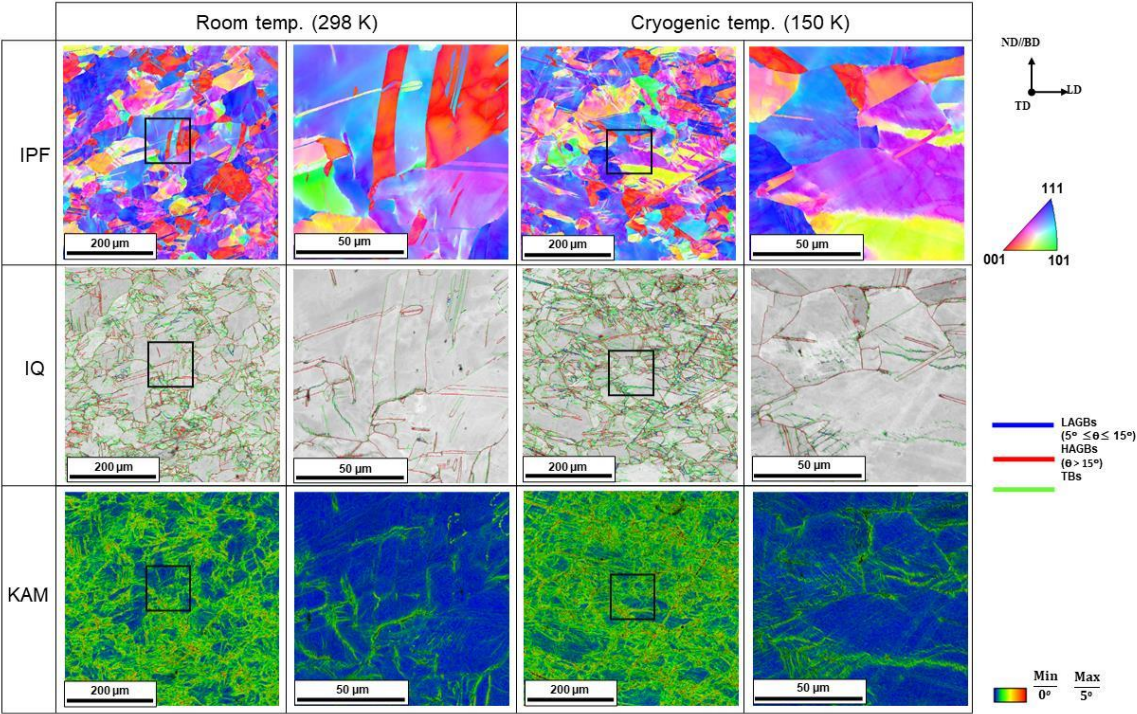


Figure 3.11 The IPF, IQ and KAM maps of deformed microstructures of HIP-treated CrCoNi MEA-SLM at engineering strain of 0.3 at room (298 K) and cryogenic (150 K) temperatures.

As shown in the KAM maps in Figs. 3.10 and 3.11, it reveals a noticeably heterogenous

KAM distribution in both the microstructures of as-built and HIP-treated CrCoNi SLM-MEA. At both temperatures, the as-built specimen shows an intragranular orientation spread while the HIP treated one reveals the locally intense KAM distribution as shown in the enlarged microstructure. It is obtained that the average KAM in the as-built decreases from 1.85 ± 0.88 to 1.64 ± 0.85 with the decrease in temperature. In contrast, the HIP-treated one shows an increase in average KAM from 1.19 ± 0.75 to 1.33 ± 0.74 as the temperature decreases. It indicates that when the HIP treated CrCoNi SLM-MEA is subjected to the deformation at low temperature, larger plastic deformation can be accommodated which contributes to the improved elongation to fracture at cryogenic temperature.

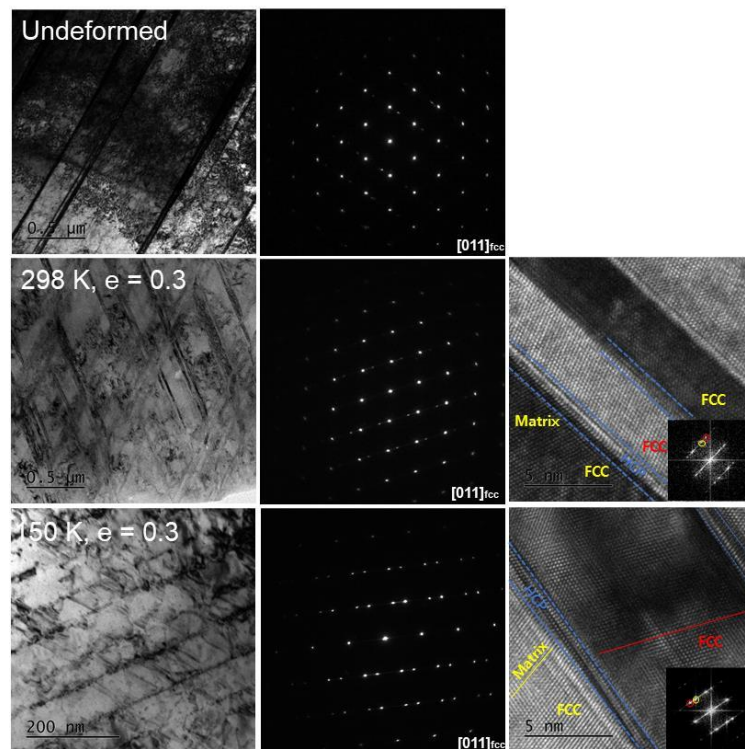


Figure 3.12 TEM micrographs showing microstructural evolution with strain ($e = 0.3$) at room (298 K) and cryogenic (150 K) of as-built specimen.

To investigate the elementary deformation mechanisms of the CrCoNi MEA-SLM and identify the microstructural features responsible for the increase of yield strength and elongation to fracture as well as WHR at cryogenic (150 K) temperature, additional TEM investigations

were conducted with as-built and HIP treated specimens at undeformed and deformed states. TEM images showing the microstructural evolutions of as-built and HIP treated CrCoNi MEA-SLM are given in Figs. 3.12 and 3.13, respectively. Micrographs in the left columns are bright-field images showing the deformation twinning, while those in the middle are selected area diffraction (SAD) patterns showing diffraction spots from the matrix and extra spots characteristic of deformation twinning. Images in the right column are high-resolution TEM images (HR-TEM) showing the size of deformation twinning. Compared to the undeformed state, the dislocation density increases after deformation because the deformation is accommodated by the dislocation slide. The dislocations are piled up against grain boundaries and play a role of strong obstacles to dislocation movement. Deformation twinning is also observed in both as-built and HIP-treated CrCoNi MEA-SLM, which may enhance the work hardening rate through the dynamic Hall-Petch effect and delay the occurrence of necking, resulting in the increase in elongation to fracture [40]. In addition, the nucleation of HCP structures is observed. Most of the HCP structures nucleate within nano twins, leading to the formation of nanotwin-HCP lamellae, which be very effective barriers for dislocation slip [11]. This observation is in good agreement with the low stacking fault energy of the CrCoNi alloy reported in the literature ($22 \pm 4 \text{ mJ/m}^2$) [45]. Thus, the deformation of as-built and HIP treated CrCoNi MEA-SLM is initially accommodated by the glide of dislocations, then the onset of deformation twinning occurs at higher strains. However, the deformation twinning at 150 K is found to be thinner than those observed at 298 K, leading to enhancement of both strength and WHR as well as elongation to fracture at cryogenic temperature as reported in the previous study [40].

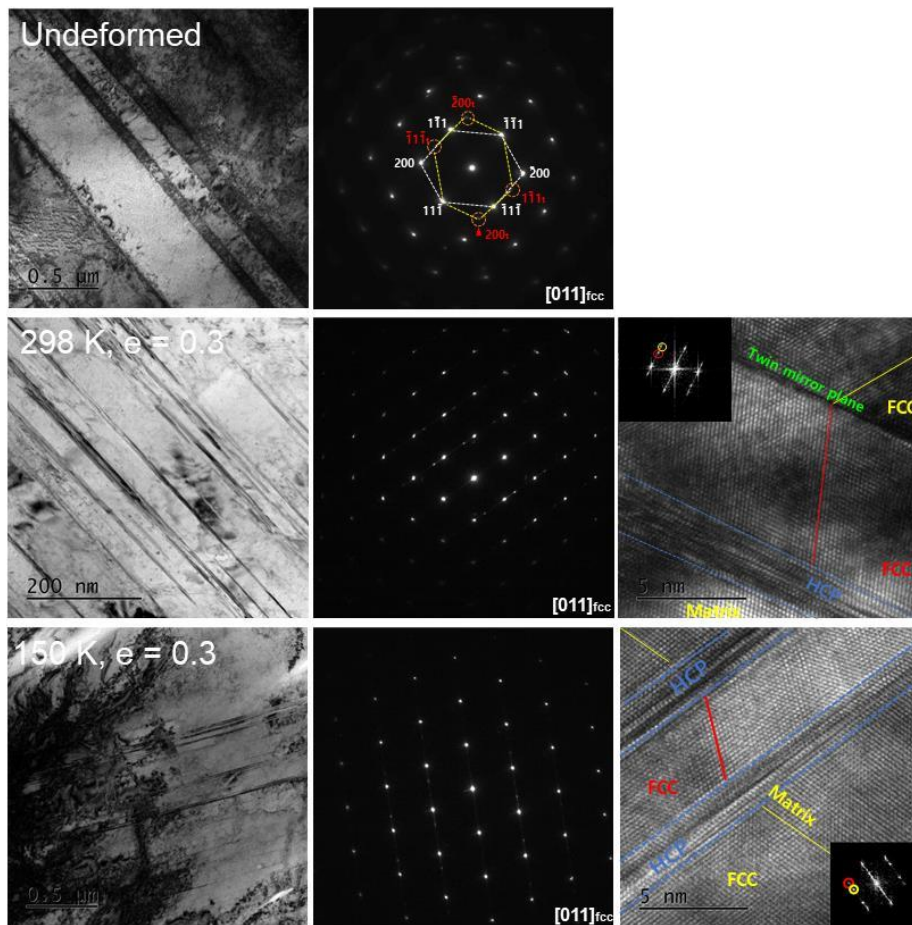


Figure 3.13 TEM micrographs showing microstructural evolution with strain ($e = 0.3$) at room (298 K) and cryogenic (150 K) of HIP-treated specimen.

4. CONCLUSION

In this study, the CrCoNi medium entropy alloy (MEA) was prepared by additive manufacturing of selective laser melting (SLM) with hot isostatic pressing (HIP). The microstructures and mechanical properties of as-built and HIP-treated CrCoNi MEA-SLM were investigated at room (298 K) and cryogenic (150 K) temperatures. The finite element simulation of the melting pool was performed to estimate the melt pool size and temperature field around the melt pool during the SLM process. The microstructure-property correlation, as well as the governing deformation mechanism in the as-built and HIP-treated CrCoNi MEA-SLM, were examined by EBSD and TEM. The following conclusions were drawn.

- (i) The laser power (P) and scanning speed (v) have a significant effect on the surface morphology of the as-built specimen characterized by the relative density. It reveals that the optimal processing parameters ($P = 240$ W, $v = 533$ mm/s) are obtained with the relative density of 99.97% at an energy density of 150.1 J/mm³.
- (ii) The as-built CrCoNi MEA-SLM shows relatively higher strength compared to the HIP-treated one due to the greater initial dislocation density as the result of rapid heating (5.8×10^6 K/s) and cooling rates (3.2×10^6 K/s) according to the simulation results of temperature history at a material point during the SLM process. After the HIP, however, the CrCoNi MEA-SLM exhibits improved elongation to fracture owing to the significant decrease of pores and cleavages as revealed in the fractography analysis.
- (iii) At 150 K, both as-built and HIP-treated CrCoNi MEA-SLM show a noticeable increase in not only strength but also ductility compared to room temperature (298 K). The TEM analysis reveals that the excellent cryogenic strength and ductility combination of CrCoNi MEA processed by SLM is attributed to the synergistic effects of dislocation glide, deformation twinning and their interactions.

Furthermore, the pronounced dislocation activity and deformation twinning are responsible for the steady work hardening of the HIP-treated CrCoNi MEA-SLM.

(iv) Moreover, a comprehensive comparison of the mechanical properties of CrCoNi MEASLM with the other MEAs reveals the potential possibility of HIP in additive manufacturing of CrCoNi MEA with exceptional mechanical properties at cryogenic temperature.

REFERENCE

- [1] M.-H. Tsai, J.-W. Yeh, High-Entropy Alloys: A Critical Review, *Materials Research Letters* 2(3) (2014) 107-123.
- [2] S. Wang, Atomic Structure Modeling of Multi-Principal-Element Alloys by the Principle of Maximum Entropy, *Entropy* 15(12) (2013) 5536-5548.
- [3] Y.F. Ye, Q. Wang, J. Lu, C.T. Liu, Y. Yang, High-entropy alloy: challenges and prospects, *Materials Today* 19(6) (2016) 349-362.
- [4] J. Rackwitz, Q. Yu, Y. Yang, G. Laplanche, E.P. George, A.M. Minor, R.O. Ritchie, Effects of cryogenic temperature and grain size on fatigue-crack propagation in the medium-entropy CrCoNi alloy, *Acta Materialia* 200 (2020) 351-365.
- [5] K. Feng, Y. Zhang, Z. Li, C. Yao, L. Yao, C. Fan, Corrosion properties of laser cladded CrCoNi medium entropy alloy coating, *Surface and Coatings Technology* 397 (2020).
- [6] G. Laplanche, A. Kostka, O.M. Horst, G. Eggeler, E.P. George, Microstructure evolution and critical stress for twinning in the CrMnFeCoNi high-entropy alloy, *Acta Materialia* 118 (2016) 152-163.
- [7] Z. Wu, H. Bei, G.M. Pharr, E.P. George, Temperature dependence of the mechanical properties of equiatomic solid solution alloys with face-centered cubic crystal structures, *Acta Materialia* 81 (2014) 428-441.
- [8] G. Laplanche, A. Kostka, C. Reinhart, J. Hunfeld, G. Eggeler, E.P. George, Reasons for the superior mechanical properties of medium-entropy CrCoNi compared to high-entropy CrMnFeCoNi, *Acta Materialia* 128 (2017) 292-303.
- [9] B. Gludovatz, A. Hohenwarter, K.V. Thurston, H. Bei, Z. Wu, E.P. George, R.O. Ritchie, Exceptional damage-tolerance of a medium-entropy alloy CrCoNi at cryogenic temperatures, *Nat Commun* 7 (2016) 10602.

- [10] W. Woo, J.S. Jeong, D.K. Kim, C.M. Lee, S.H. Choi, J.Y. Suh, S.Y. Lee, S. Harjo, T. Kawasaki, Stacking Fault Energy Analyses of Additively Manufactured Stainless Steel 316L and CrCoNi Medium Entropy Alloy Using In Situ Neutron Diffraction, *Sci Rep* 10(1) (2020) 1350.
- [11] J. Miao, C.E. Slone, T.M. Smith, C. Niu, H. Bei, M. Ghazisaeidi, G.M. Pharr, M.J. Mills, The evolution of the deformation substructure in a Ni-Co-Cr equiatomic solid solution alloy, *Acta Materialia* 132 (2017) 35-48.
- [12] K. Jiang, T. Ren, G. Shan, T. Ye, L. Chen, C. Wang, F. Zhao, J. Li, T. Suo, Dynamic mechanical responses of the Al_{0.1}CoCrFeNi high entropy alloy at cryogenic temperature, *Materials Science and Engineering: A* 797 (2020).
- [13] Q. Ding, X. Fu, D. Chen, H. Bei, B. Gludovatz, J. Li, Z. Zhang, E.P. George, Q. Yu, T. Zhu, R.O. Ritchie, Real-time nanoscale observation of deformation mechanisms in CrCoNi-based medium- to high-entropy alloys at cryogenic temperatures, *Materials Today* 25 (2019) 21-27.
- [14] G. Kardys, Factors to Consider When 3D Printing or Additive Manufacturing Metal Parts. <https://insights.globalspec.com/article/7447/factors-to-consider-when-3d-printing-or-additive-manufacturing-metal-parts>, December 19, 2017).
- [15] Z. Ma, Q. Zhai, K. Wang, G. Chen, X. Yin, Q. Zhang, L. Meng, S. Wang, L. Wang, Fabrication of Fe-based metallic glass reinforced FeCoNiCrMn high-entropy alloy through additive manufacturing: mechanical property enhancement and corrosion resistance improvement, *Journal of Materials Research and Technology* 16 (2022) 899-911.
- [16] Q. Jiang, P. Zhang, J. Tan, Z. Yu, Y. Tian, S. Ma, D. Wu, Influence of the microstructure on mechanical properties of SLM additive manufacturing Fe-based bulk metallic glasses, *Journal of Alloys and Compounds* 894 (2022).
- [17] H. Hotz, M. Zimmermann, S. Greco, B. Kirsch, J.C. Aurich, Additive manufacturing of functionally graded Ti-Al structures by laser-based direct energy deposition, *Journal of*

Manufacturing Processes 68 (2021) 1524-1534.

[18] X. Yang, R.A. Barrett, N.M. Harrison, S.B. Leen, A physically-based structure-property model for additively manufactured Ti-6Al-4V, *Materials & Design* 205 (2021).

[19] M. Zhang, X. Zhou, D. Wang, L. He, X. Ye, W. Zhang, Additive manufacturing of in-situ strengthened dual-phase AlCoCuFeNi high-entropy alloy by selective electron beam melting, *Journal of Alloys and Compounds* 893 (2022).

[20] X. Qiu, Microstructure and corrosion properties of Al₂CrFeCo CuNiTi high entropy alloys prepared by additive manufacturing, *Journal of Alloys and Compounds* 887 (2021).

[21] H.-S. Park, D.-S. Nguyen, Study on Flaking Behavior in Selective Laser Melting Process, *Procedia CIRP* 63 (2017) 569-572.

[22] Z. Zhang, Y. Wu, L. Bhatta, C. Li, B. Gan, C. Kong, Y. Wang, H. Yu, Mechanical properties and microstructure evolution of a CrCoNi medium entropy alloy subjected to asymmetric cryorolling and subsequent annealing, *Materials Today Communications* 26 (2021).

[23] B. Han, C. Zhang, K. Feng, Z. Li, X. Zhang, Y. Shen, X. Wang, H. Kokawa, R. Li, Z. Wang, P.K. Chu, Additively manufactured high strength and ductility CrCoNi medium entropy alloy with hierarchical microstructure, *Materials Science and Engineering: A* 820 (2021).

[24] I. Rosenthal, R. Shneck, A. Stern, Heat treatment effect on the mechanical properties and fracture mechanism in AlSi10Mg fabricated by additive manufacturing selective laser melting process, *Materials Science and Engineering: A* 729 (2018) 310-322.

[25] M. Khomutov, P. Potapkin, V. Cheverikin, P. Petrovskiy, A. Travyanov, I. Logachev, A. Sova, I. Smurov, Effect of hot isostatic pressing on structure and properties of intermetallic NiAl–Cr–Mo alloy produced by selective laser melting, *Intermetallics* 120 (2020).

[26] Q. Yu, C. Wang, G. Yang, Y. Ren, N. Liu, Y. Liang, C. Dong, Influence of Cr/Mo ratio on microstructure and mechanical properties of the Ni-based superalloys fabricated by laser additive manufacturing, *Journal of Alloys and Compounds* 894 (2022).

- [27] Z. Zhao, L. Li, W. Yang, Y. Zeng, Y. Lian, Z. Yue, A comprehensive study of the anisotropic tensile properties of laser additive manufactured Ni-based superalloy after heat treatment, *International Journal of Plasticity* 148 (2022).
- [28] M. Ghayoor, K. Lee, Y. He, C.-h. Chang, B.K. Paul, S. Pasebani, Selective laser melting of 304L stainless steel: Role of volumetric energy density on the microstructure, texture and mechanical properties, *Additive Manufacturing* 32 (2020).
- [29] H. Rao, S. Giet, K. Yang, X. Wu, C.H.J. Davies, The influence of processing parameters on aluminium alloy A357 manufactured by Selective Laser Melting, *Materials & Design* 109 (2016) 334-346.
- [30] M.T. Tran, T.H. Nguyen, D.-K. Kim, W. Woo, S.-H. Choi, H.W. Lee, H. Wang, J.G. Kim, Effect of hot isostatic pressing on the cryogenic mechanical properties of CrCoNi medium entropy alloy processed by direct energy deposition, *Materials Science and Engineering: A* 828 (2021).
- [31] J.M. Park, J. Choe, J.G. Kim, J.W. Bae, J. Moon, S. Yang, K.T. Kim, J.-H. Yu, H.S. Kim, Superior tensile properties of 1%C-CoCrFeMnNi high-entropy alloy additively manufactured by selective laser melting, *Materials Research Letters* 8(1) (2019) 1-7.
- [32] B. Gludovatz, A. Hohenwarter, D. Catoor, E.H. Chang, E.P. Geore, A fracture-resistant high-entropy alloy for cryogenic applications, *Science* 345(6201) (2014) 1153-1158.
- [33] J.M. Park, J. Moon, J.W. Bae, J. Jung, S. Lee, H.S. Kim, Effect of annealing heat treatment on microstructural evolution and tensile behavior of Al_{0.5}CoCrFeMnNi high-entropy alloy, *Materials Science and Engineering: A* 728 (2018) 251-258.
- [34] W. Lu, X. Luo, Y. Yang, B. Huang, Hall-petch relationship and heterogeneous strength of CrCoNi medium-entropy alloy, *Materials Chemistry and Physics* 251 (2020).
- [35] I. Moravcik, J. Cizek, Z. Kovacova, J. Nejezchlebova, M. Kitzmantel, E. Neubauer, I. Kubena, V. Hornik, I. Dlouhy, Mechanical and microstructural characterization of powder

metallurgy CoCrNi medium entropy alloy, *Materials Science and Engineering: A* 701 (2017) 370-380.

[36] F. Weng, Y. Chew, Z. Zhu, X. Yao, L. Wang, F.L. Ng, S. Liu, G. Bi, Excellent combination of strength and ductility of CoCrNi medium entropy alloy fabricated by laser aided additive manufacturing, *Additive Manufacturing* 34 (2020).

[37] A. Gali, E.P. George, Tensile properties of high- and medium-entropy alloys, *Intermetallics* 39 (2013) 74-78.

[38] Y.O. Kuzminova, D.G. Firsov, S.A. Dagesyan, S.D. Konev, S.N. Sergeev, A.P. Zhilyaev, M. Kawasaki, I.S. Akhatov, S.A. Evlashin, Fatigue behavior of additive manufactured CrFeCoNi medium-entropy alloy, *Journal of Alloys and Compounds* 863 (2021).

[39] F. Haftlang, H.S. Kim, A perspective on precipitation-hardening high-entropy alloys fabricated by additive manufacturing, *Materials & Design* 211 (2021).

[40] M. Schneider, G. Laplanche, Effects of temperature on mechanical properties and deformation mechanisms of the equiatomic CrFeNi medium-entropy alloy, *Acta Materialia* 204 (2021).

[41] X. Li, H.J. Willy, S. Chang, W. Lu, T.S. Heng, J. Ding, Selective laser melting of stainless steel and alumina composite: Experimental and simulation studies on processing parameters, microstructure and mechanical properties, *Materials & Design* 145 (2018) 1-10.

[42] Z. Qiu, C. Yao, K. Feng, Z. Li, P.K. Chu, Cryogenic deformation mechanism of CrMnFeCoNi high-entropy alloy fabricated by laser additive manufacturing process, *International Journal of Lightweight Materials and Manufacture* 1(1) (2018) 33-39.

[43] J. Kwon, J. Lee, H.S. Kim, Constitutive modeling and finite element analysis of metastable medium entropy alloy, *Materials Science and Engineering: A* 840 (2022).

[44] P.L.J. Conway, T.P.C. Klaver, J. Steggo, E. Ghassemali, High entropy alloys towards industrial applications: High-throughput screening and experimental investigation, *Materials*

Science and Engineering: A 830 (2022).

[45] W. Woo, J.S. Jeong, D.K. Kim, C.M. Lee, S.H. Choi, J.Y. Suh, S.Y. Lee, S. Harjo, T. Kawasaki, Stacking Fault Energy Analyses of Additively Manufactured Stainless Steel 316L and CrCoNi Medium Entropy Alloy Using In Situ Neutron Diffraction, *Scientific Reports* 10(1) (2020) 1350.